Excited State Non-Adiabatic Dynamics of Pyrrole: A Time-Resolved Photoelectron Spectroscopy and Ab Initio Quantum Dynamics Study

Guorong Wu[†,‡,§], Simon P. Neville[‖], Oliver Schalk[†,⊥], Taro Sekikawa[†,#], Michael N. R. Ashfold[⊤], Graham A. Worth[‖], and Albert Stolow[†,¶]

[†]National Research Council of Canada, 100 Sussex Drive, Ottawa, Ontario K1A 0R6, Canada
[¶]Departments of Chemistry and Physics, University of Ottawa, 10 Marie Curie, Ottawa, Ontario, K1N 6N5, Canada
[‡]State Key Laboratory of Molecular Reaction Dynamics, Dalian Institute of Chemical Physics, Chinese Academy of Sciences, Dalian, Liaoning 116023, China
[§]Synergetic Innovation Center of Quantum Information and Quantum Physics, University of Science and Technology of China, Hefei, Anhui 230026, China
[‖]School of Chemistry, University of Birmingham, Edgbaston, Birmingham, B15 2TT, United Kingdom
[⊥]Department of Physics, AlbaNova University Center, Stockholm University, Roslagstullbacken 21, 109 61 Stockholm, Sweden
[⊤]School of Chemistry, University of Bristol, Bristol, BS8 1TS, United Kingdom
[#]Department of Applied Physics, Hokkaido University, Kita-13 Nishi-8, Kita-ku, Sapporo 060-8628, Japan

October 16, 2014

Abstract

The dynamics of pyrrole excited at wavelengths in the range 242-217 nm are studied using a combination of time-resolved photoelectron spectroscopy (TRPES) and wavepacket propagations performed using the multiconfigurational time-dependent Hartree (MCTDH) method. Excitation close to the origin of pyrrole's electronic spectrum, at 242 and 236 nm, is found to result in an ultrafast decay of the system from the ionization window on a single timescale of less than 20 fs. This behaviour is explained fully by assuming the system to be excited to the $A_2(\pi\sigma^*)$ state, in accord with previous experimental and theoretical studies. Excitation at shorter wavelengths has previously been assumed to result predominantly in population of the bright $A_1(\pi\pi^*)$ and $B_2(\pi\pi^*)$ states. We here present time-resolved photoelectron spectra at a pump wavelength of 217 nm alongside detailed quantum dynamics calculations that, together with a recent reinterpretation of pyrrole's electronic spectrum (S. P. Neville and G. A. Worth, J. Chem. Phys., **140**, 034317 (2014)), suggest that population of the $B_1(\pi\sigma^*)$ state (hitherto assumed to be optically dark) may occur directly when pyrrole is excited at energies in the near part of its UV spectrum. The $B_1(\pi\sigma^*)$ state is found to decay on a timescale of less than 20 fs, by both N-H dissociation and internal conversion to the $A_2(\pi\sigma^*)$ state.

1 Introduction

Pyrrole is a prototypical heteroaromatic molecule and, as such, the understanding of its electronic structure and photochemistry has attracted much attention from both experiment and theory [1–21]. In turn, the photochemisry of small heteroaromatic molecules has itself been the subject of recent interest in part due to their being experimentally and computationally tractable models for the chromophores of a range of important biomolecules, including aromatic amino acids and the DNA bases. Such molecules are remarkable for their vanishingly small fluorescence quantum yields, a property that implicates the existence of efficient non-radiative decay mechanisms connecting the excited and ground electronic states of these molecules. Central to the understanding of this behaviour has been the theoretical studies of Domcke and co-workers [2, 3]. In these studies, a general mechanism for non-radiative decay was proposed that invokes the population of low-lying singlet states of bound $3s/\pi\sigma^*$ character. These states are predominantly of $3s$ Rydberg-type character in the vicinity of the Franck-Condon (FC) point. However, due to vibronic coupling to higher-lying, dissociative valence-type states, the adiabatic potentials of these states are typically quasi-bound with respect to the stretching of a heteroatom-hydride (X-H) bond, exhibiting typically modest barriers to X-H dissociation. Hence population of such states following

electronic excitation may facilitate non-radiative decay. These so-called $3s/\pi\sigma^*$ states (from here on referred to as $\pi\sigma^*$ states for brevity) typically have either zero or close-to-zero oscillator strengths around the FC point, but are in general vibronically coupled to energetically proximate states of $\pi\pi^*$ character that are optically bright.

Most studies of the excited state dynamics of pyrrole to date have been concerned with excitation at energies underlying the first band in the molecule's electronic spectrum, which lies in the range 5.5 to 6.5 eV [22]. For reference, the relative ordering of the states spanning this energy range is shown in Figure 1a. The explanation of the experimental data and, thus, the derived picture of the photodissociation and nonadiabatic dynamics of its excited states, has been based on various assignments of the UV absorption spectrum. It is generally agreed that the weak tail in the spectrum appearing below 5.5 eV is attributable to the "optically forbidden" $A_2(\pi\sigma^*)$ Rydberg state. However, the characterization of the the spectrum at higher energies has been complicated by the existence of a high density of vibronically coupled states [23–27]. It was generally believed that the majority of the intensity in the first band of the spectrum arises due to excitation to the $B_2(\pi\pi^*)$ state, with pronounced resonances superimposed resulting from excitations to $3p$-type Rydberg states [22, 27]. Utilising this interpretation of the spectrum, a large number of experimental studies of the excited state dynamics of pyrrole have been performed.

In the energy domain, experimental studies have focused mainly on measurement of the H product translational energy and angular distributions. Using photofragment translational spectroscopy (PTS), Blank *et al.* found upon excitation at 193 and 248 nm, that the H elimination channel is the main dissociation channel [1]. Later, higher energy-resolution experiments [4–8, 15] in the wavelength range 193.3-254.0 nm observed two components in the H product translational energy distributions: a "fast" component with a higher, sharp kinetic energy distribution and a "slow" component with a lower, broad kinetic energy distribution. A picture was proposed as follows: upon the approach of the wavepacket to the CI between the $3s/\pi\sigma^*$ and ground states, the wavepacket either evolves to the ground state and results in a statistical dissociation of the hot ground state, leading to nascent H-atoms with lower kinetic energies, or evolves diabatically leading to a direct cleavage of the N-H bond to yield H-atoms with higher kinetic energies. At shorter pump wavelengths within this range, pyrrole was believed to be excited to the $B_2(\pi\pi^*)$ state, which decays to the $A_2(3s/\pi\sigma^*)$ state and then follows the dynamics of the latter.

In the time domain, ultrafast time-resolved studies have provided direct measurements of the excited state lifetimes and of the appearance of the H-atom products. Lippert *et al.* [9] carried out the first ultrafast time-resolved measurement in which the $A_2(3s/\pi\sigma^*)$ state was excited at 250 nm and the H-atom products were

probed as a function of pump-probe delay using 2+1 resonance enhanced multiphoton ionization. Two time constants were derived from the H^+ signal profile: τ_1=110±80 fs and τ_2=1.1±0.5 ps. The shorter time constant was attributed to the direct cleavage of the N-H bond on the repulsive $A_2(3s/\pi\sigma^*)$ state potential, the longer to the statistical dissociation of the hot ground state following internal conversion (IC) to the ground state. Montero *et al.* [18] measured excited state lifetimes directly by detecting time-resolved total ion yields, following excitation in the 265-217 nm range. They concluded that the wavepacket prepared in the $A_2(3s/\pi\sigma^*)$ state at longer wavelength evolves out of the ionization window with a timescale of 15±3 fs, and that the wavepacket prepared in the $B_2(\pi\pi^*)$ state at shorter pump wavelengths decays to the lower $A_2(3s/\pi\sigma^*)$ state on a timescale of 19±3 fs. Roberts *et al.* [19] studied the H-elimination dynamics of pyrrole using a combination of ultrafast time-resolved ion yield and time-resolved velocity map ion imaging techniques in the excitation wavelength range 250-200 nm. Following direct excitation to the $A_2(3s/\pi\sigma^*)$ state at 250 nm, a much longer time constant of 126±28 fs was observed, which was attributed to tunneling out of the quasi-bound part of the $A_2(3s/\pi\sigma^*)$ state potential in the vertical Franck-Condon region, followed by direct dissociation along the repulsive surface of the $A_2(3s/\pi\sigma^*)$ state. At 238 nm, direct excitation to the $A_2(3s/\pi\sigma^*)$ state, leading to N-H dissociation, was observed to occur with a time constant of 46±22 fs. Upon initial population of the $B_2(\pi\pi^*)$ state at 200 nm, a rapid $B_2(\pi\pi^*)$/$A_2(3s/\pi\sigma^*)$/N-H fission process was proposed to occur within 52±12 fs. At this wavelength, statistical unimolecular H-atom elimination from a vibrationally hot ground state formed after relaxation of the excited electronic states was also observed, but with a time constant of 1.0±0.4 ns.

Theoretical studies have been devoted to electronic structure calculations, the characterization of the CIs between different electronic states, and dynamical simulation using quantum-classical trajectory based methods and fully quantum mechanical wavepacket propagation calculations [10, 12–14, 20, 21, 28]. These are generally in good agreement with experiment, and provide very detailed information on the nonadiabatic decay channels of the electronically excited states.

The results of all previous experimental studies of the photoinduced dynamics of pyrrole have been analysed using the assumption that excitation at energies higher than ∼5.7 eV should result in population of the $B_2(\pi\pi^*)$ state, in accord with previous assignments of the spectrum. However, a recent re-calculation of the UV absorption by Neville and Worth (NW) has put the previous assignments in doubt [29]. In this study, wavepacket propagations performed using the multiconfigurational time-dependent Hartree (MCTDH) method were used to calculate the spectrum. The analysis of the calculated spectrum showed that most of the intensity at energies between 5.5 and 6.0 eV is attributable to vibronic states that result from the strong nonadiabatic coupling of the bright $A_1(\pi\pi^*)$ and $B_2(\pi\pi^*)$

valence states to the lower-lying $B_1(\pi\sigma^*)$ and $A_2(\pi 3p_z)$ Rydberg-type states. Most importantly, with regards to the work presented in this paper, the vibronic states underlying the peak centred at 5.7 eV in the spectrum were found to be mainly of $B_1(\pi\sigma^*)$ character, implicating the significant role played by intensity borrowing from the transitions to the bright $\pi\pi^*$ states by the $B_1(\pi\sigma^*) \leftarrow S_0$ transition. Hence, the conclusion was drawn that excitation close to 5.7 eV should result predominantly in transition to vibronic states associated with the $B_1(\pi\sigma^*)$ state, in contradiction to assignments used in previous studies that did not properly take into account the vibronic coupling of the states underlying pyrrole's UV absorption spectrum.

Prompted by the re-assignment of the pyrrole's electronic spectrum made by NW, in this paper we re-examine the dynamics of pyrrole excited in the near part of its UV spectrum, at wavelengths of 242, 236 and 217 nm, combining TRPES and *ab initio* quantum dynamics calculations. Good agreement was obtained between the experimental and computational results. In the following, we describe the TRPES method used for our experimental study of the excited state dynamics of pyrrole. We present our detailed quantum dynamics calculations and use these to rationalize the experimental observations. Detailed discussion of the excited state dynamics ensues, followed by conclusions.

2 Methods

2.1 Experimental Method

We briefly describe our femtosecond time-resolved magnetic bottle photoelectron spectrometer experiments, detailed elsewhere [30]. Three different pump wavelengths were used: 217 nm (60-100 nJ), 236 nm (0.6-0.9 μJ), and 242 nm (1.1-1.5 μJ). The probe laser was fixed at 266 nm (0.8-5.0 μJ). Femtosecond laser pulses were obtained from a Ti:Sapphire regenerative amplifier (Coherent, Legend, 800 nm). Part of the output ($\sim$700 μJ) was used for harmonic generation to produce a 266 nm laser pulse. A second part ($\sim$700 μJ) was used to pump a TOPAS (optical parametric amplifier, Light Conversion) system. The idler from the TOPAS was doubled with a BBO crystal and mixed with an 800 nm ($\sim$460 μJ) beam in a second BBO crystal. The resulting sum frequencies were doubled in a third BBO crystal to generate 217 nm. For 236 and 242 nm, the signal from the TOPAS was mixed with an 800 nm ($\sim$460 μJ) beam in a BBO crystal. The resulting sum frequencies were doubled in a second BBO crystal. UV pulses were individually recompressed using CaF_2 prism pairs, combined collinearly on a dichroic mirror, and then gently focused using an f/125 spherical reflective mirror to intersect a seeded molecular beam in the interaction region of a magnetic bottle spectrome-

ter. Time delays between pump and probe pulses were scanned using a computer-controlled stepper motor. Liquid sample of pyrrole (Sigma-Aldrich, $\geq$98%) was loaded into the cartridge of a 1 kHz Even-Lavie pulsed valve, and helium carrier gas of 3-4 bar generated the supersonic molecular beam. The pump pulse excited the molecules from their ground state into an excited state whereupon the delayed probe pulse produces photoelectrons via one-photon ionization. Photoelectron spectra arising from the pump and the probe laser alone, and at negative time delays (i.e., the probe preceding the pump) were also recorded. The sum of the single colour photoelectrons, or the signal at negative delays were subtracted in order to correct for background photoelectrons generated from single colour multiphoton ionizations. Pump-probe time delays were scanned back and forth multiple times to minimize any small hysteresis effects and/or spatial laser drift.

Electron kinetic energy calibration and time zero overlap of the two laser pulses were achieved using the well-characterized two-photon nonresonant ionization of nitric oxide [31, 32]. This also served to measure the cross-correlation (i.e., instrumental response function) between the pump and the probe laser pulses. The delay dependent curve of the electron yield was fitted, based on the approximation that both pump and probe laser pulses have a Gaussian profile, yielding a cross-correlation of 0.142 ps for 217 nm + 266 nm, 0.135 ps for 236 nm + 266 nm, and 0.153 ps for 242 nm + 266 nm.

2.2 Computational Methods

2.2.1 The Model Hamiltonian

We choose to represent the molecular Hamiltonian $\hat{H}$ in a quasi-diabatic electronic basis $\{|\sigma\rangle\}$ (from here on referred to more succinctly, although not entirely rigorously, as a diabatic basis):

$$\begin{aligned}\hat{H} &= \sum_{\sigma,\sigma'=1}^{n_s} |\Phi_\sigma\rangle H_{\sigma\sigma'} \langle\Phi_{\sigma'}| \\ &= \sum_{\sigma=1}^{n_s} |\Phi_\sigma\rangle T_{\sigma\sigma} \langle\Phi_\sigma| + \sum_{\sigma,\sigma'=1}^{n_s} |\Phi_\sigma\rangle W_{\sigma\sigma'} \langle\Phi_{\sigma'}| .\end{aligned} \tag{1}$$

The primary reasons for the adoption of a diabatic basis are two-fold: (i) in a diabatic representation the elements of the potential matrix W are smooth functions of the nuclear coordinates q, thus making them amenable to approximation by simple analytic functions, and; (ii) the troublesome non-adiabatic coupling terms $\left\langle \sigma \left| \frac{\partial}{\partial q} \right| \sigma' \right\rangle$, which in the adiabatic representation become singular at the intersection of two states, are rendered sufficiently small to warrant their neglect.

The electronic basis chosen comprises the six states $A_1(S_0)$, $A_2(\pi\sigma^*)$, $B_1(\pi\sigma^*)$, $A_2(\pi 3p_z)$, $A_1(\pi\pi^*)$ and $B_2(\pi\pi^*)$. The nuclear coordinates used correspond to the set of ground state normal modes of the pyrrolyl radical fragment, denoted by $\{Q_\alpha : \alpha = 1,\ldots,3N-9\}$, and the spherical polar coordinates of the hydrogen atom of the N-H bond, denoted H_d, taken relative to the position of the nitrogen atom at the FC point, X_N^{FC}, of the parent pyrrole molecule, denoted $r = (R,\theta,\phi)$. Here, R denotes the distance of H_d from X_N^{FC}, while θ and ϕ correspond, respectively, to the in- and out-of-plane angles formed by the N-H_d bond relative to the plane defined by the C-N-C vertex. The model diabatic potential matrix $W(Q,r)$ used is taken from reference 29. Briefly, this model corresponds to the representation of the potential in the space spanned by the modes Q, θ and ϕ by a vibronic coupling Hamiltonian [33, 34], and the representation of the diabatic potentials along the N-H dissociation coordinate R using simple analytic functions with appropriate asymptotic behaviour. The coupling between the subset of bound degrees of freedom (Q,θ,ϕ) and dissociative degree of freedom R is dealt with by taking the parameters entering into the expansion of the potential with respect to the bound degrees of freedom to be functions of R that exhibit the correct asymptotic behaviour. The reader is directed to reference 29 for a comprehensive description of this model.

2.2.2 Quantum Dynamics Calculations

Wavepacket propagations were performed using the MCTDH method [35, 36] as implemented in the Heidelberg MCTDH package [37]. The so-called multi-set formalism was adopted [38, 39], for which the wavefunction ansatz reads

$$\left|\Psi(Q_1,\ldots,Q_p,t)\right\rangle = \sum_{\sigma=1}^{n_s} \left|\Psi^{(\sigma)}(Q_1,\ldots,Q_p,t)\right\rangle \left|\sigma\right\rangle, \tag{2}$$

where $\left|\Psi^{(\sigma)}(Q_1,\ldots,Q_p,t)\right\rangle$ denotes the nuclear wavefunction associated with the electronic state $\left|\sigma\right\rangle$. Each nuclear wavefunction is expanded as

$$\left|\Psi^{(\sigma)}(Q_1,\ldots,Q_p,t)\right\rangle = \sum_{j_1^\sigma=1}^{n_1^\sigma} \cdots \sum_{j_p^\sigma=1}^{n_p^\sigma} A^{(\sigma)}_{j_1^\sigma\ldots j_p^\sigma}(t) \prod_{\kappa=1}^{p} \varphi^{(\kappa,\sigma)}_{j_\kappa^\sigma}(Q_\kappa,t). \tag{3}$$

Here, the p multi-dimensional logical coordinates Q_κ each correspond to a composite of d_κ physical coordinates q_ν:

$$Q_\kappa = \left(q_{\nu_1^\kappa},\ldots,q_{\nu_{d_\kappa}^\kappa}\right). \tag{4}$$

Equations of motion for the expansion coefficients $A^{(\sigma)}_{j_1^\sigma \cdots j_p^\sigma}$ and so-called single-particle functions (SPFs) $\varphi^{(\kappa,\sigma)}_{j_\kappa^\sigma}$ are derived from the Dirac-Frenkel variational principle, leading to an optimal description of the evolving wavepacket for a given choice of basis. The time-dependent SPFs are in turn expanded in terms of a time-independent basis, chosen as a discrete variable representation (DVR) [40].

In order to avoid the use of a prohibitively long grid for the dissociative degree of freedom R, the model Hamiltonian is modified via the addition of a complex absorbing potential (CAP) [41], which we denote by $\Omega(R)$,

$$\hat{H} \rightarrow \hat{H} + \sum_{\sigma=1}^{n_s} |\sigma\rangle \, \Omega(R) \, \langle\sigma| \,, \tag{5}$$

where

$$\Omega(R) = -i\eta\Theta(R-R_c)(R-R_c)^m. \tag{6}$$

Here, η corresponds to a strength parameter and $\Theta(R-R_c)$ to the Heaviside step function centred at a value of R of R_c. With a suitably chosen CAP strength η and order m, a CAP placed sufficiently far into the asymptotic part of the potential will result in the annihilation of those components of the wavepacket that enter into it.

To simulate excitation of the system to an electronic state $|\sigma\rangle$, the initial state $|\Psi(0)\rangle$ is chosen as

$$|\Psi(0)\rangle = \{|\sigma\rangle \langle 1| + h.c.\} \, |\Psi_{GS}\rangle \,, \tag{7}$$

where $|\Psi_{GS}\rangle$ denotes the ground state of the Hamiltonian, determined using the method of relaxation (propagation of an initial guess wavepacket in negative imaginary time) [42]. That is, we take our initial states to correspond to vertical excitation to the electronic state of interest.

2.2.3 Calculation of Dissociation Probabilities

We define the probability of N-H dissociation at a time t, $p_d(t)$, as the expectation value of the projector onto the subspace for which $R > R_d$, where R_d is a value of R that is in the asymptotic part of the potential, i.e.,

$$p_d(t) = \langle\Psi(t)|\Theta(R-R_d)|\Psi(t)\rangle \,. \tag{8}$$

We here work with a value of R_d corresponding to an N-H bond length of 6.4 a.u, a value at which both the $A_2(\pi\sigma^*)$ and $B_1(\pi\sigma^*)$ state potentials are just within their asymptotic regions. The quantity $p_d(t)$ is calculated by integrating over time the flux $F(t;R_d)$ passing through a dividing surface placed at R_d, which is calculated as the expectation value of the flux operator $\hat{F}(R_d)$,

$$\hat{F}(R_d) = i\left[\hat{T}_N, \Theta(R - R_d)\right], \tag{9}$$

where $\hat{T}_N$ denotes the nuclear kinetic energy operator. State-resolved probabilities of dissociation were calculated by integrating over time the expectation value of the projected flux operator $\hat{F}^{(\sigma)}(R_d)$, defined as

$$\hat{F}^{(\sigma)}(R_d) = \hat{P}_\sigma \hat{F}(R_d)\hat{P}_\sigma, \tag{10}$$

where $\hat{P}_\sigma = |\sigma\rangle\langle\sigma|$ is the projector onto the σth electronic state.

2.2.4 Calculation of Photoionization Cross-Sections

We consider ionization from a neutral N-electron electronic state $|\Phi_I^{(N)}\rangle$ to an ionized state corresponding to an antisymmetrized product of an (N-1)-electron cationic state $|\Phi_\alpha^{(N-1)}\rangle$ and the photoelectron orbital ψ_k. Assuming vertical ionization and the applicability of Fermi's golden rule, the probability of single-photon ionization, $P_I^{\alpha k}$, is given by

$$P_I^{\alpha k}(E) \propto \left|\left\langle \Phi_I^{(N)} \middle| \mu \middle| \Phi_\alpha^{(N-1)} \psi_k \right\rangle\right|^2 \delta(E - E_I^\alpha - E_k). \tag{11}$$

Here, E is the energy of the applied laser pulse, E_I^α is the vertical energy difference between the cationic state $|\Phi_\alpha^{(N-1)}\rangle$ and the neutral state $|\Phi_I^{(N)}\rangle$, $E_k = k^2/2$ is the kinetic energy of the photoelectron, and μ is the molecular dipole operator. Assuming a zero overlap between the neutral state and the free electron, we obtain

$$P_I^{\alpha k}(E) \propto \left|\left\langle \phi_{I\alpha}^D \middle| \mu \middle| \psi_k \right\rangle\right|^2 \delta(E - E_I^\alpha - E_k), \tag{12}$$

where the one-electron quantity $\phi_{I\alpha}^D$ is a so-called Dyson orbital, defined as the overlap between the neutral and cationic states:

$$\phi_{I\alpha}^D = \sqrt{N} \int \Phi_I^{(N)}(r_1, \ldots, r_N)\Phi_\alpha^{(N-1)}(r_1, \ldots, r_{N-1})dr_1 \cdots dr_{N-1}. \tag{13}$$

We assume that the photoelectron interacts with the cationic core through a point charge Coulomb potential such that the continuum states ψ_k are described using Coulomb partial waves. Using the ezDyson code [43], the photoionisation matrix elements $\left\langle \phi_{Ik}^D \middle| \mu \middle| \psi_k \right\rangle$ are evaluated numerically on a grid and averaged isotropically over molecular orientations.

Dyson orbitals corresponding to ionization from both the $A_2(\pi\sigma^*)$ and $B_1(\pi\sigma^*)$ neutral states to each of the D_0 and D_1 cationic states were calculated within the equation-of-motion coupled-cluster with single and double excitations (EOM-CCSD) framework, with the same N-electron Hartree Fock reference state being used for all calculations. The aug-cc-pVDZ basis was used for all calculations. All

calculations were performed using the Q-Chem 4.2 program [44]. The geometry used in the calculation of all Dyson orbitals corresponds to the FC point, optimized at the MP2/aug-cc-pVDZ level using the Gaussian 03 set of programs [45].

3 Results

3.1 Experimental Results

The TRPES spectra of pyrrole at pump wavelengths of 217, 236 and 242 nm are shown in Figures 2-4. The excited states prepared by the pump laser pulses, at all three wavelengths, decay on timescales faster than the pump-probe cross-correlation. For pump wavelengths of 236 and 242 nm, only one time constant seems involved. At 217 nm, the photoelectrons with kinetic energies in the range 1.1-1.6 eV show a delayed rise, in contrast to those at higher kinetic energies, indicating a sequential process and that there are two components involved. The energetic limits for ionization to the D_0 and D_1 states of the cation, calculated using previously reported ionization potentials of 8.21 and 9.2 eV for the D_0 and D_1 states, respectively [46], are also indicated in the lower panels in Figures 2-4. For pump wavelengths of 236 and 242 nm, the photoelectron spectra comprise two parts, corresponding to ionization to the ground and first excited states of the cation. The photoelectron spectrum at 217 nm is more diffuse and covers the kinetic energy range corresponding to both the ground and first excited states of the cation.

In order to extract more detailed information from these TRPES spectra, a 2D global least-squares method was employed to simultaneously fit data at all time delays and photoelectron kinetic energies using the Levenberg-Marquardt algorithm [47]. The kinetic model used to fit the TRPES data comprises the cross-correlation and multiple exponential decays and can be written as the following equation:

$$S(\varepsilon_k, \Delta t) = \left[\sum_i D_i(\varepsilon_k) \exp\left(-\frac{\Delta t}{\tau_i} \right) \right] \otimes g(\Delta t). \tag{14}$$

Here, ε_k is the kinetic energy of the emitted photoelectrons, and Δt the time delay between pump and probe laser pulses. The $D_i(\varepsilon_k)$ is the ith decay associated spectrum (DAS) which represents the energy-resolved amplitude of the component having the time constant τ_i. The DASs are closely related to the energy-resolved photoionization cross sections of the electronic states involved in the dynamics [47], and $g(\Delta t)$ is the cross-correlation function which was determined separately.

The DASs and time constants derived from the fit are shown beneath the figures of the TRPES spectra and in Table 1, respectively. There is only one time constant involved for pump wavelengths of 236 (19 fs) and 242 nm (12 fs), and there are two time constants involved for the pump wavelength of 217 nm: τ_1=13 fs and τ_2=29 fs. The error bars listed in Table 1 for the time constants are based on the uncertainties of the time zeros, the cross-correlations, and the statistical errors of the data. The origin and physical interpretation of these time constants will be discussed in Section 4.

3.2 Theoretical Results

From a consideration of previously calculated vertical excitation energies and the analysis of pyrrole's electronic absorption spectrum given by NW, we proceed by assuming that excitation at 217 nm results predominantly in excitation to the $B_1(\pi\sigma^*)$ state, enhanced via intensity borrowing from the $A_1(\pi\pi^*) \leftarrow A_1(S_0)$ transition. Excitation at both 236 nm and 242 nm should result in population of the $A_2(\pi\sigma^*)$ state, simply by virtue of there being predicted to exist no other electronic states in this energy range. As such, wavepacket propagations simulating excitation to each of these two states were performed.

With regards to the short term dynamics of a system starting in a state indexed by σ, the importance of a given nuclear degree of freedom may be judged through consideration of the gradients of the diabatic potential elements $W_{\sigma\sigma'}$ ($\sigma' = 1, \ldots, n_s$) with respect to that degree of freedom. Through an analysis of the gradients of the off-diagonal potential elements, it is found that the modes Q_{19} (asymmetric C-H stretching) and Q_{21} (ring stretching) couple more strongly than any other degrees of freedom (by an order of magnitude) the states $A_2(\pi\sigma^*)$ and $B_1(\pi\sigma^*)$. There are found to exist large gradients of both the $A_2(\pi\sigma^*)$ and $B_1(\pi\sigma^*)$ state diabatic potentials with respect to the modes Q_{11} (ring breathing) and Q_{16} (ring stretching). Additionally, significant gradients of the $B_1(\pi\sigma^*)$ state diabatic potential exist with respect to the modes Q_5 (ring breathing) and Q_{10} (ring breathing). As such, these six pyrrolyl normal modes were chosen for inclusion in the wavepacket propagation calculations, simulating excitation to both the $A_2(\pi\sigma^*)$ and $B_1(\pi\sigma^*)$ states. Additionally, the N-H stretching mode R and the N-H out-of-plane bending mode ϕ were also chosen to be included, on account of their description of the large amplitude motion of the dissociating hydrogen atom.

3.2.1 Dynamics Following Excitation to the $A_2(\pi\sigma^*)$ State

The dynamics of pyrrole following excitation to the $A_2(\pi\sigma^*)$ state was calculated using an eight-mode model comprising the nuclear degrees of freedom mentioned

in Section 3.2. A propagation time of 750 fs was used, and all other details of the calculation are displayed in Table 2.

Illustrated in Figure 5 are the calculated diabatic state populations and time-cumulated N-H dissociation probabilities following vertical excitation to the $A_2(\pi\sigma^*)$ state. Population is found to remain predominantly in the initially excited state, and non-negligible transfer of population is found to occur only to the $B_1(\pi\sigma^*)$ state, with the probability of population of this state being calculated to be 0.06 after 750 fs.

We observe an initial period of rapid N-H dissociation in the initially excited $A_2(\pi\sigma^*)$ state, with a probability of dissociation of $\sim$0.52 being attained after the first 50 fs. Thereon after a slower rate of dissociation is observed, with the calculated probability of dissociation reaching 1.0 after 750 fs. The existence of two timescales for dissociation in the $A_2(\pi\sigma^*)$ state may be attributed to the nature of the excitation scheme employed. Specifically, vertical excitation of the ground state wavepacket to the $A_2(\pi\sigma^*)$ state was performed. Hence, the initial wavepacket used can be seen to correspond to a linear combination of the vibrational states of the $A_2(\pi\sigma^*)$ state, each being weighted by their Franck-Condon factors. As such, there exist components of the initial wavepacket that exist with energies both above and below the barrier to dissociation on the $A_2(\pi\sigma^*)$ state potential. We attribute the initial period of fast N-H dissociation to the direct dissociation of those components of the wavepacket lying above the barrier to dissociation, whilst the ensuing slower period of dissociation is attributed to the tunneling of the lower-energy components of the wavepacket through the barrier to dissociation.

Timescales for these two mechanisms of N-H dissociation were determined through the fitting of the following simple model to the calculated total time-cumulated probability of N-H dissociation (illustrated in Figure 5 (b)):

$$p(t) = \Theta(t-t_c)\left\{1 - a\exp\left(-\frac{t-t_c}{\tau_1}\right) - (1-a)\exp\left(-\frac{t-t_c}{\tau_2}\right)\right\}. \qquad (15)$$

Here, the two timescales τ_1 and τ_2 are used to account for the possibility of both direct and tunneling mechanisms of N-H dissociation being operative. The constant t_c corresponds to the time taken by the wavepacket to first reach the dissociation limit, and $\Theta(t-t_c)$ denotes the Heaviside step function centred at t_c. Using a simple simplex optimiser, the following parameter values were determined: a=0.64, τ_1=35 fs, τ_2=133 fs, t_c=15 fs. The fitted value of a, the coefficient corresponding to direct dissociation, implies that after vertical excitation tunneling through the barrier to dissociation plays an important, though not dominant role.

3.2.2 Dynamics Following Excitation to the $B_1(\pi\sigma^*)$ State

The dynamics of pyrrole following excitation to the $B_1(\pi\sigma^*)$ state was modeled using the same eight-mode model as used to describe excitation to the $A_2(\pi\sigma^*)$ state. A propagation time of 750 fs was used, and all other details of the calculation are displayed in Table 2.

As there exists more than one decay pathway in the $B_1(\pi\sigma^*)$ state (N-H dissociation and internal conversion to the $A_2(\pi\sigma^*)$ state), in addition to the state-resolved dissociation probabilities, we here consider the state-resolved expectation values of the projector onto the interaction region,

$$p_I^{(\sigma)}(t) = \left\langle \Psi(t) \middle| \hat{P}_\sigma \Theta(R_d - R) \hat{P}_\sigma \middle| \Psi(t) \right\rangle, \tag{16}$$

as a suitable measure of the rate of decay of the population of the FC region of the initially excited $B_1(\pi\sigma^*)$ state and the subsequently populated $A_2(\pi\sigma^*)$ state. The expectation value $p_I^{(\sigma)}$ can be seen to correspond to a measure of proportion of the population in the state indexed by σ that is in the subspace for which $R < R_d$. Choosing a value of R_d that corresponds to an N-H bond length that is only just in the asymptotic part of the potential (here taken as 6.4 a.u.), the $p_I^{(\sigma)}$ provide a measure of the proportion of the population of each state that has not reached the dissociation limit.

Shown in Figure 6 are the diabatic state populations, time-cumulated probabilities of N-H dissociation and expectation values of the projectors $p_I^{(\sigma)}$ onto the interaction regions of both the $B_1(\pi\sigma^*)$ and $A_2(\pi\sigma^*)$ states calculated following excitation to the $B_1(\pi\sigma^*)$ state. It is found that dissociation in the $B_1(\pi\sigma^*)$ state and internal conversion to the $A_2(\pi\sigma^*)$ state both contribute to the decay of the population of the FC region of the initially excited state, with 34% of the wavepacket being found to undergo dissociation in the $B_1(\pi\sigma^*)$ state and the remaining 66% undergoing internal conversion to the $A_2(\pi\sigma^*)$ state.

From the calculated expectation values $p_I^{(\sigma)}$, timescales for decay of the population of the FC region in the $B_1(\pi\sigma^*)$ state and in the subsequently populated $A_2(\pi\sigma^*)$ state were estimated as follows. Functions of the form $\exp(-t/\tau)$ were fitted to the set of values $\left\{ p_I^{(\sigma)} : t \in [0, 750] \right\}$ for the $B_1(\pi\sigma^*)$ state and $\left\{ p_I^{(\sigma)} : t \in [20, 750] \right\}$ for the $A_2(\pi\sigma^*)$ state, t=20 fs being the time at which transfer of population to the $A_2(\pi\sigma^*)$ state is essentially complete. From this we estimate lifetimes of 19 fs for decay from the initially excited $B_1(\pi\sigma^*)$ state and of 61 fs for decay from the subsequently populated $A_2(\pi\sigma^*)$ state.

4 Discussion

4.1 Assignment of the Fitted Time Constants

The TRPES data for pyrrole at all three wavelengths are well simulated by the model described in Equation 14. There is only one time constant derived for pyrrole pumped at long wavelengths: 19 fs and 12 fs for pump wavelengths of 236 and 242 nm, respectively. According to the electronic absorption spectrum and the electronic structure calculations, the $A_2(\pi\sigma^*)$ state is the only state accessible at these pump wavelengths. Therefore, it is very straightforward to assign these single time constants to the lifetime of the $A_2(\pi\sigma^*)$ state.

For the pump wavelength of 217 nm, there are two non-trivial time constants involved: τ_1=13 fs and τ_2=29 fs. The DAS associated with τ_2 has a positive value over the whole photoelectron spectrum, while that of τ_1 has a negative value over a broad range of electron kinetic energies where the DAS of τ_2 has large amplitudes. The negative amplitudes obtained from the fits can only originate from a sequential process: the electronic state excited by the pump laser pulse has a lifetime of τ_1 and decays to a lower electronic state which has a lifetime of τ_2. According to the electronic absorption spectrum and dynamics simulations, pyrrole is mainly excited to the $B_1(\pi\sigma^*)$ state at 217 nm and subsequently decays to the $A_2(\pi\sigma^*)$ state. Therefore, the timescales τ_1 and τ_2 are assigned to the lifetimes of the $B_1(\pi\sigma^*)$ and $A_2(\pi\sigma^*)$ states, respectively.

Further support of the assignments of these time constants is provided by Dyson orbitals and photoionisation cross-sections corresponding to ionization from the $A_2(\pi\sigma^*)$ and $B_1(\pi\sigma^*)$ states, calculated as detailed in Section 2.2.3. The vertical excitation energies (VEEs) of the D_0 and D_1 states obtained at the EOM-CCSD/aug-cc-pVDZ level are 8.15 and 8.98 eV, respectively, in agreement with previously reported values [46, 48]. Shown in Table 3 are the norms of the calculated Dyson orbitals. Also shown in this table are estimates of the kinetic energies of the photoelectrons produced following vertical ionization from the $A_2(\pi\sigma^*)$ and $B_1(\pi\sigma^*)$ states using a probe wavelength of 266 nm, calculated using the value of 5.70 eV for the VEE of the $B_1(\pi\sigma^*)$ state, estimated from the analysis of pyrrole's electronic spectrum given in Reference 29, and VEE for the $A_2(\pi\sigma^*)$ state determined previously using high-level CASPT2 calculations [29]. Taking the norm of a given Dyson orbital to be proportional to the cross-section for the corresponding vertical ionization process, it is predicted that the $A_2(\pi\sigma^*)$ state will ionize preferentially to the D_0 state of the cation, producing photoelectrons with kinetic energies estimated to be around 1.57 eV. This appears to be consistent with the fitted DAS for excitation at 217 nm associated with the timescale τ_2, shown in Figure 4. The photoionization cross-sections derived from this DAS are most significant in the region proximate with the estimated photoelectron kinetic ener-

gies for ionization from the $A_2(\pi\sigma^*)$ state to the D_0 state, suggesting preferential ionization to the ground cationic state.

In contrast, from an analysis of Dyson orbitals alone, the $B_1(\pi\sigma^*)$ state is predicted to ionize to both the D_0 and D_1 states without preference, producing photoelectrons with estimated kinetic energies of around 2.27 and 1.44 eV, respectively. Further information is provided by the photoionization cross-sections calculated using the photoionization matrix elements $\langle \phi_{Ik}^D | \mu | \psi_k \rangle$ corresponding to ionization from the $B_1(\pi\sigma^*)$ state, shown in Figure 7 plotted against various values of the probe laser pulse energy. It is predicted that at the threshold for ionization from the $B_1(\pi\sigma^*)$ state to both the D_0 and D_1 ($E_{pump} \sim 3.3$ eV), there is a slight preference for ionization to the D_1 state, with the ratio of the two cross-sections taking a value of 1.2. However, upon increasing the pump energy to that used experimentally (4.66 eV), it is predicted that ionization should occur preferentially to the lower-lying D_0 state, with a ratio of calculated cross-sections of 1.7. This appears to be consistent with the fitted DAS for excitation at 217 nm. The photoionization cross-sections derived from the DAS associated with the time constant τ_1, assigned to decay of the population of the FC region of the initially excited $B_1(\pi\sigma^*)$ state, have significant non-zero amplitude over a range of kinetic energies. However, they are greatest in value at higher photoelectron energies in the region proximate with the estimated photoelectron kinetic energies for ionization from the $B_1(\pi\sigma^*)$ state to the D_0 state: this implies that there is a preference for ionization to the ground state of the cation. Thus, the analysis of the photoionization cross-sections supports the proposed mechanism of initial excitation to the $B_1(\pi\sigma^*)$ state, followed by internal conversion to the $A_2(\pi\sigma^*)$ state and non-radiative decay in the latter state.

4.2 Non-Radiative Decay Dynamics

At 236 and 242 nm, the initially excited state is ascribed as the $A_2(\pi\sigma^*)$ state. The quantum dynamics calculations performed simulating the vertical excitation to the $A_2(\pi\sigma^*)$ state are found to be dominated by two mechanisms for N-H dissociation: (i) direct dissociation of the high-energy components of the wavepacket that lie above the barrier to dissociation, and; (ii) tunneling through the barrier to dissociation of the components of the wavepacket that lie below the barrier to dissociation. Accordingly, we observe two timescales for N-H dissociation in the $A_2(\pi\sigma^*)$ state: 35 fs and 133 fs, corresponding, respectively, to direct dissociation and tunneling. The timescale for direct dissociation is in good agreement with the time constants of 12±10 fs and 19±10 fs derived from the TRPES spectra recorded following excitation at 242 nm and 236 nm, respectively. Hence, we conclude that excitation at wavelengths of 242 nm and 236 nm results in excitation to energy levels lying near to or above the barrier to dissociation in the $A_2(\pi\sigma^*)$ state,

leading to prompt N-H dissociation. The smaller time constant derived (both experimentally and theoretically) is in good agreement with the timescale of 46±22 fs for N-H dissociation measured using time-resolved velocity map imaging by Roberts *et al.* following excitation at 238 nm [19], while the larger time constant of 133 fs calculated for tunneling is in excellent agreement with the timescale of 128±28 fs for N-H dissociation reported by the same authors following excitation near the $A_2(\pi\sigma^*)$ state origin at 250 nm.

At 217 nm, the initially excited state is assigned to the $B_1(\pi\sigma^*)$ state. According to the dynamics simulations, both rapid N-H dissociation in the initially excited state and internal conversion to the $A_2(\pi\sigma^*)$ state are found to occur. A timescale of 19 fs is calculated for the decay of the wavepacket from the FC region in the $B_1(\pi\sigma^*)$ state, whilst the population reaching the $A_2(\pi\sigma^*)$ state is found to undergo dissociation on a 61 fs timescale. These values compare well to the time constants of τ_1=13±10 fs and τ_2 =29±10 fs derived from the TRPES spectra recorded following excitation at 217 nm, and thus lend credence to the proposition that excitation at 217 nm should result in population of the $B_1(\pi\sigma^*)$ state and subsequent internal conversion to the lower-lying $A_2(\pi\sigma^*)$ state. The proposed non-radiative decay pathways open following excitation at 217 nm are shown schematically in Figure 1b.

5 Conclusions

Knowledge of the identity of the electronic transitions underlying a molecule's electronic absorption spectrum is essential to unravel experimental observations concerning its excited state dynamics. Analysis of the electronic spectrum of pyrrole has proven difficult, by virtue of the existence of a high density of strongly vibronically coupled electronic states. Recent quantum dynamics calculations employing a newly developed model Hamiltonian that accounts for the vibronic coupling between the low-lying states of pyrrole shed new light on the transitions underlying the first band in the electronic spectrum of pyrrole [29], and have implicated the significant, but previously neglected role played by states of $3s/\pi\sigma^*$ and $3p$ Rydberg character in the molecule's spectrum. Guided by this, the dynamics of pyrrole following excitation at energies in the near part of the molecule's electronic spectrum have been re-examined using a combination of TRPES, quantum dynamics calculations and photoionization cross-section calculations.

TRPES spectra recorded following excitation near the origin of the electronic spectrum, reveal single time constants of 12 fs and 19 fs for excitation at 242 nm and 236 nm, respectively. These time constants are assigned to direct dissociation of the wavepacket excited above the barrier to dissociation in the $A_2(\pi\sigma^*)$ state. Corroboration of this assignment comes from quantum dynamics calcula-

tions performed that simulate vertical excitation to the $A_2(\pi\sigma^*)$ state and from which a timescale of 35 fs is derived for direct dissociation of the components of the wavepacket lying above the barrier to dissociation.

In light of the assignment of the electronic spectrum made in reference 29, excitation at 217 nm is postulated to result in population of the $B_1(\pi\sigma^*)$ state via intensity borrowing from the $A_1(\pi\pi^*) \leftarrow A_1(S_0)$ transition. The TRPES spectrum recorded following excitation at 217 nm is found to yield two timescales for decay, τ_1=13 fs and τ_2=29 fs, and reveals a sequential process corresponding to the decay of an initial state with a lifetime τ_1 to a lower-lying state which has a lifetime of τ_2. This is in agreement with the notion of excitation at 217 nm resulting in the population of the $B_1(\pi\sigma^*)$ state and subsequent internal conversion to the lower-lying $A_2(\pi\sigma^*)$ state. This assertion is found to be in good agreement with the results of quantum dynamics calculations simulating excitation to the $B_1(\pi\sigma^*)$ state, from which timescales of 19 fs and 61 fs are calculated for decay of the population of the FC regions of the initially excited state and of the subsequently populated $A_2(\pi\sigma^*)$ state, respectively. The assignment of the fitted decay channels to the dynamics of specific excited states was independently corroborated by the calculation of Dyson orbital norms and photoionization matrix elements for the various ionization transitions involved. We anticipate that *ab initio* quantum dynamics simulations will continue to play an important role in deciphering absorption spectra and excited state ultrafast dynamics experiments in polyatomic molecules.

Table 1: 2D globally fitted time constants from the TRPES data. The pump and probe laser wavelengths (photon energies) used and the corresponding cross-correlations are also as indicated.

Pump/probe (nm) (pump/probe (eV))	Cross-correlation (fs)	τ_1 (fs)	τ_2 (fs)
241.5/266.3 (5.13/4.66)	142	12±10	
236.2/266.4 (5.25/4.65)	135	19±10	
217.0/266.4 (5.71/4.65)	153	13±10	29±10

Table 2: Computational details of the wavepacket propagations. The discrete variable representation (DVR) types exp and HO correspond to exponential [49] and harmonic oscillator [35] DVRs, respectively. N_i, N_j are the number of primitive DVR functions used to describe each particle. n_i are the number of single-particle functions used for each state.

	Particle	DVR type	N_i, N_j	$n_1, n_2, n_3, n_4, n_5, n_6$
Excitation to $A_2(\pi\sigma^*)$				
	R	exp	71	3, 8, 7, 4, 3, 2
	ϕ	exp	80	3, 5, 5, 4, 3, 2
	$\{Q_5, Q_{10}\}$	HO, HO	20, 25	3, 9, 7, 4, 3, 2
	$\{Q_{11}, Q_{16}\}$	HO, HO	25, 25	3, 8, 7, 4, 3, 2
	$\{Q_{19}, Q_{21}\}$	HO, HO	30	3, 7, 7, 4, 3, 2
Excitation to $B_1(\pi\sigma^*)$				
	R	exp	71	3, 7, 7, 4, 3, 2
	ϕ	exp	80	3, 5, 5, 4, 3, 2
	$\{Q_5, Q_{10}\}$	HO, HO	20, 25	3, 7, 7, 4, 3, 2
	$\{Q_{11}, Q_{16}\}$	HO, HO	25, 25	3, 7, 7, 4, 3, 2
	$\{Q_{19}, Q_{21}\}$	HO, HO	30	3, 7, 7, 4, 3, 2

Table 3: Dyson orbital norms $\left|\left|\phi^D\right|\right|$ corresponding to vertical ionization from both the S_1 ($A_2(\pi\sigma^*)$) and S_2 ($B_1(\pi\sigma^*)$) states to each of the D_0 and D_1 cation states as calculated at the EOM-CCSD/aug-cc-pVDZ level. Also shown are the estimated kinetic energies E_{el} of the photoelectrons produced following each vertical ionization process.

Transition	$\left\|\phi^D\right\|$	E_{el} (eV)
$S_1 \rightarrow D_0$	0.35	1.57
$S_1 \rightarrow D_0$	0.02	0.74
$S_2 \rightarrow D_1$	0.26	2.21
$S_2 \rightarrow D_1$	0.34	1.38

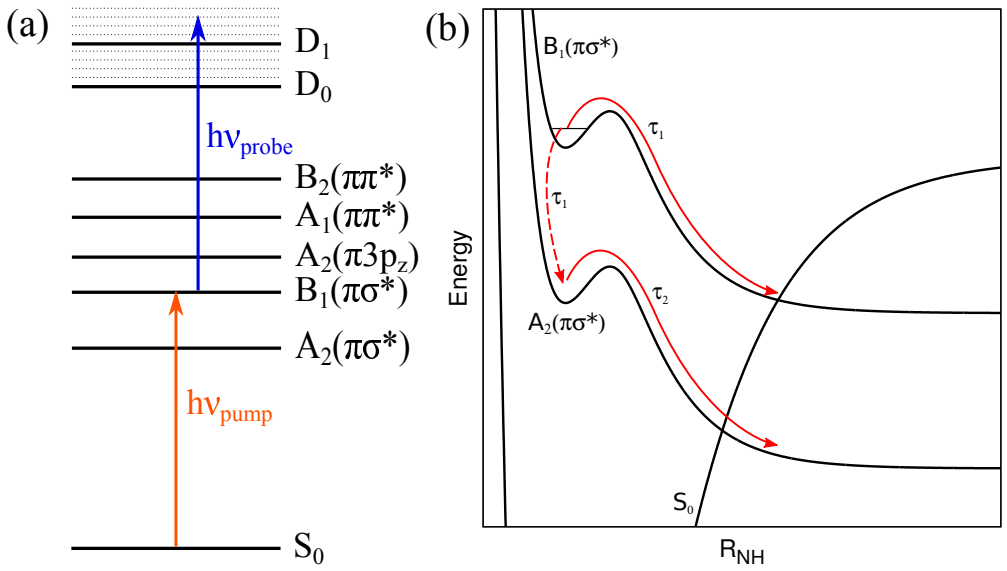

Figure 1: Schematic images depicting the proposed excited state dynamics of pyrrole following excitation at 217 nm. (a) Energy level diagram showing the ordering of the lowest neutral and cationic states of pyrrole, together with arrows representing the pump (orange) and probe (blue) fs laser pulses. (b) Schematic potential energy curves for the $A_2(\pi\sigma^*)$ and $B_1(\pi\sigma^*)$ states along the N-H dissociation coordinate. Illustrated by the red arrows are the relaxation pathways predicted to be open following population of the $B_1(\pi\sigma^*)$ state after excitation at 217 nm. Solid arrows represent dissociation pathways in the $A_2(\pi\sigma^*)$ and $B_1(\pi\sigma^*)$ states. The dashed arrow represents internal conversion from the $B_1(\pi\sigma^*)$ state to the $A_2(\pi\sigma^*)$ state. The label τ_i next to a given arrow denotes the time constant for decay associated with that pathway (see Table 1).

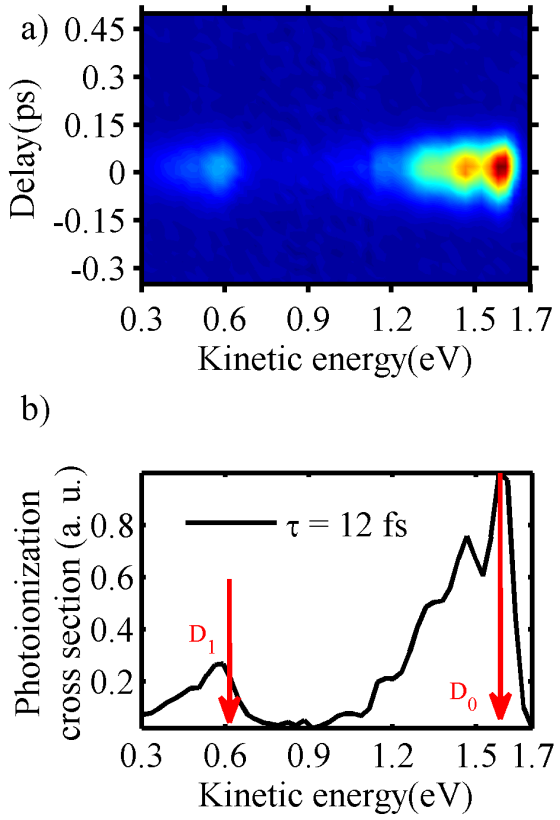

Figure 2: a) TRPES spectrum of pyrrole at a pump wavelength of 242 nm after subtracting background photoelectrons generated from single colour multiphoton ionization. b) The partial photoionization cross section derived from a 2D global least-squares fit to the data shown in a). The origins of the relevant cation electronic states are indicated by red arrows.

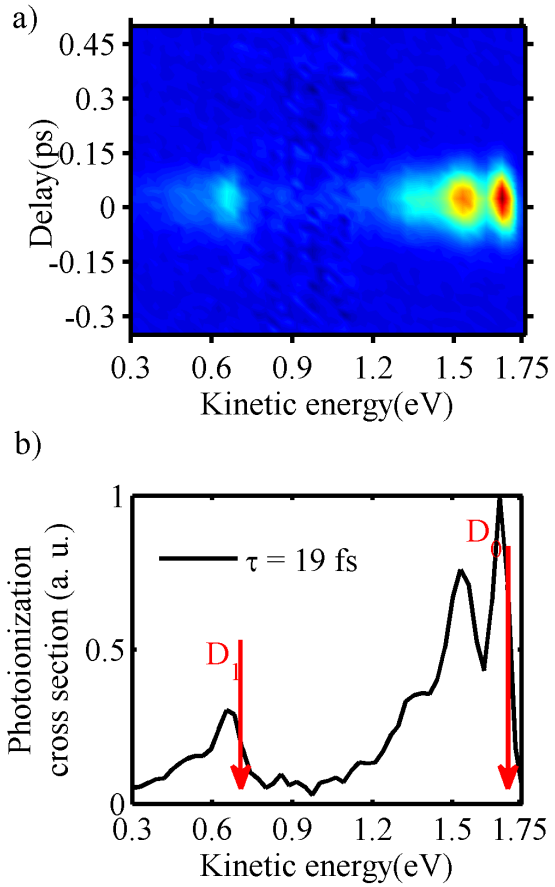

Figure 3: a) TRPES spectrum of pyrrole at a pump wavelength of 236 nm after subtracting background photoelectrons generated from single colour multiphoton ionization. b) The partial photoionization cross section derived from a 2D global least-squares fit to the data shown in a). The origins of the relevant cation electronic states are indicated by red arrows.

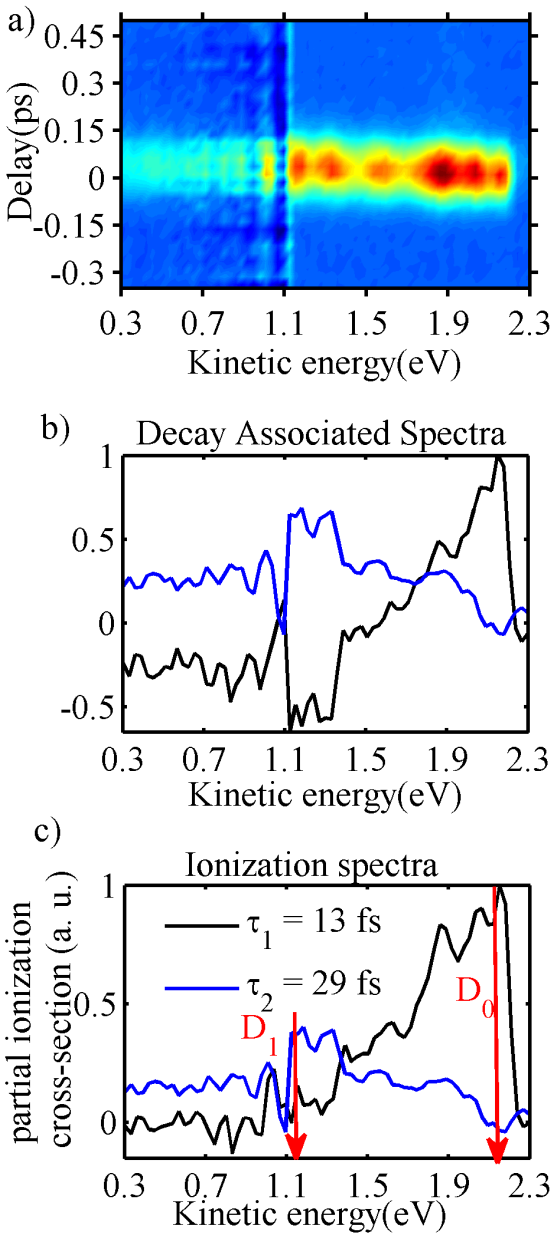

Figure 4: a) TRPES spectrum of pyrrole at a pump wavelength of 217 nm after subtracting background photoelectrons generated from single colour multiphoton ionization. b) The partial photoionization cross section derived from a 2D global least-squares fit to the data shown in a). c) Photoionization cross sections derived from the DAS assuming a two-step sequential process. The origins of the relevant cation electronic states are indicated by red arrows.

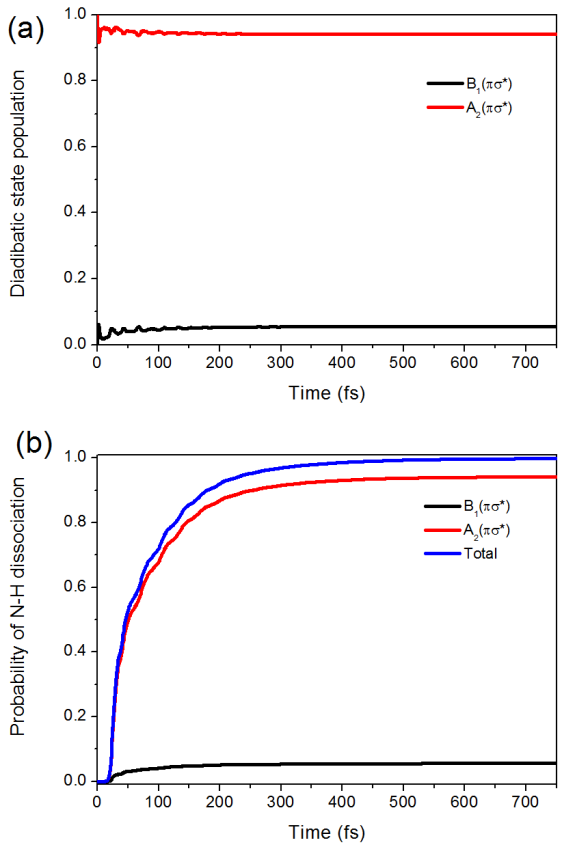

Figure 5: (a) Calculated diabatic state populations, and (b) calculated state-resolved probabilities of N-H dissociation following excitation to the $A_2(\pi\sigma^*)$ state.

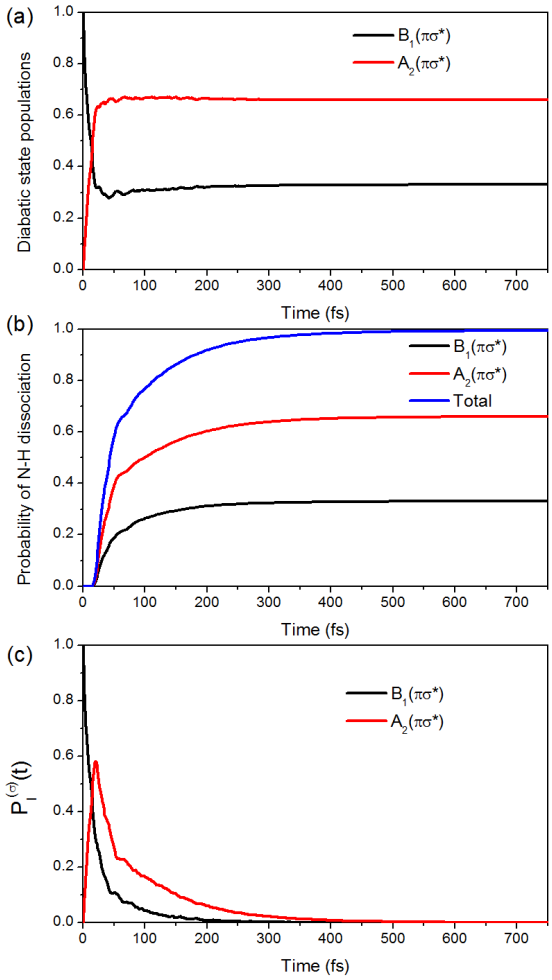

Figure 6: (a) Calculated diabatic state populations, (b) calculated probabilities of N-H dissociation following excitation to the $A_2(\pi\sigma^*)$ state, and (c) calculated values of the expectation value of the projector onto the interaction region for both the $B_1(\pi\sigma^*)$ and $A_2(\pi\sigma^*)$ states following excitation to the $B_1(\pi\sigma^*)$ state.

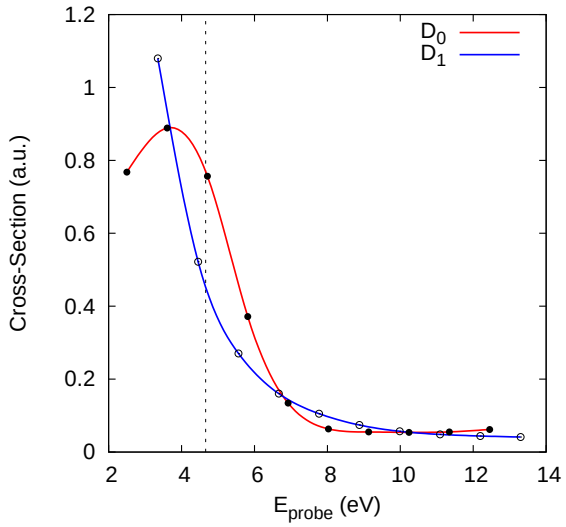

Figure 7: Calculated photoionization cross-sections corresponding to ionization from the $B_1(\pi\sigma^*)$ state to each of the D_0 (solid circles, red line) and D_1 (open circles, blue line) states of the cation at the FC point. The cross-sections are shown plotted against various values of the pump laser energy. The experimentally used probe photon energy is marked by the vertical dashed line. All quantities were estimated using Dyson orbitals calculated at the EOM-CCSD/aug-cc-pVDZ level.

References

[1] D. A. Blank, S. W. North, and Y. T. Lee. Chem. Phys. **187**, 35 (1994).

[2] A. L. Sobolewski and W. Domcke. Chem. Phys. **259**, 181 (2000).

[3] A. L. Sobolewski, W. Domcke, C. Dedonder-Lardeux, and C. Jouvet. Phys. Chem. Chem. Phys. **4**, 1093 (2002).

[4] J. Wei, A. Kuczmann, J. Riedel, F. Reneth, and F. Temps. Phys. Chem. Chem. Phys. **5**, 315 (2003).

[5] J. Wei, J. Riedel, A. Kuczmann, F. Renth, and F. Temps. Faraday Discuss. **127**, 267 (2004).

[6] B. Cronin, M. G. D. Nix, R. H. Qadiri, and M. N. R. Ashfold. Phys. Chem. Chem. Phys. **6**, 5031 (2004).

[7] B. Cronin, A. L. Devine, M. G. D. Nix, and M. N. R. Ashfold. Phys. Chem. Chem. Phys. **8**, 3440 (2006).

[8] T. N. V. Karsili, B. Marchetti, R. Mocha, and M. N. R. Ashfold. J. Phys. Chem. A **117**, 12067 (2013).

[9] H. Lippert, H. H. Ritzel, I. V. Hertel, and W. Radloff. ChemPhysChem **5**, 1423 (2004).

[10] V. Vallet, Z. Lan, S. Mahapatra, A. L. Sobolewski, and W. Domcke. J. Chem. Phys. **123**, 144307 (2005).

[11] M. N. R. Ashfold, B. Cronin, A. L. Devine, R. N. Dixon, and M. G. D. Nix. Science **312**, 1637 (2006).

[12] M. Barbatti, M. Vazdar, Adélia, M. Eckert-Maksić, and H. Lischka. J. Chem. Phys. **125**, 164323 (2006).

[13] Z. Lan, A. Dupays, V. Vallet, S. Mahapatra, and W. Domcke. J. Photochem. Photobiol. A **190**, 177 (2007).

[14] B. Sellner, M. Barbatti, and H. Lischka. J. Chem. Phys. **131**, 024312 (2009).

[15] L. Rubio-Lago, D. Zaouris, Y. Sakellariou, D. Sofikitis, T. N. Kitsopoulos, F. Wang, X. Yang, B. Cronin, A. L. Devine, G. A. King, M. G. D. Nix, M. N. R. Ashfold, and S. S. Xantheas. J. Chem. Phys. **127**, 064306 (2007).

[16] M. Vazdar, M. Eckert-Maksić, M. Barbatti, and H. Lischka. Mol. Phys. **107**, 845 (2009).

[17] M. N. R. Ashfold, G. A. King, D. Murdock, M. G. D. Nix, T. A. A. Oliver, and A. G. Sage. Phys. Chem. Chem. Phys. **12**, 1218 (2010).

[18] R. Montero, A. P. Conde, V. Ovejas, M. Fernández-Fernández, F. Castaño, J. R. V. de Aldana, and A. Longarte. J. Chem. Phys. **137**, 064317 (2012).

[19] G. M. Roberts, C. A. Williams, H. Yu, A. S. Chatterly, J. D. Young, S. Ulrich, and V. G. Stavros. Faraday Discuss. **163**, 1 (2012).

[20] M. Barbatti, J. Pittner, M. Pederzoli, U. Werner, R. Mitrić, V. B. Koutecký, and H. Lischka. Chem. Phys. **375**, 26 (2010).

[21] K. Saita, M. G. D. Nix, and D. V. Shalashilin. Phys. Chem. Chem. Phys. **15**, 16227 (2013).

[22] M. H. Palmer, I. C. Walker, and M. F. Guest. Chem. Phys. **238**, 179 (1998).

[23] L. Serrano-Andrés, M. Merchán, I. Nebot-Gil, B. Roos, and M. Fülscher. J. Am. Chem. Soc. **115**, 6184 (1993).

[24] H. Nakano, T. Tsuneda, and T. Hashimoto. J. Chem. Phys. **104**, 2312 (1996).

[25] O. Christiansen, J. Gauss, J. F. Stanton, and P. Jorgensen. J. Chem. Phys. **111**, 525 (1999).

[26] J. Wan, J. Meller, M. Hada, M. Ehara, and H. Nakatsuji. J. Chem. Phys. **113**, 7853 (2000).

[27] B. O. Roos, P. A. Malmqvist, V. Molina, L. Serrano-Andrés, and M. Merchán. J. Chem. Phys. **116**, 7526 (2002).

[28] M. H. Palmer and P. J. Wilson. Mol. Phys. **101**, 2391 (2003).

[29] S. P. Neville and G. A. Worth. J. Chem. Phys. **140**, 034317 (2014).

[30] S. Lochbrunner, J. J. Larsen, J. P. Shaffer, M. Schmitt, T. Schultz, J. G. Underwood, and A. Stolow. J. Electron Spectrosc. Relat. Phenom. **112**, 183 (2000).

[31] G. W. Bethke. J. Chem. Phys. **31**, 662 (1959).

[32] G. K. Jarvis, M. Evans, C. Y. Ng, and K. Mitsuke. J. Chem. Phys. **111**, 3058 (1999).

[33] H. Köppel, W. Domcke, and L. S. Cederbaum. Adv. Chem. Phys. **57**, 59 (1984).

[34] L. S. Cederbaum, H. Köppel, and W. Domcke. Int. J. Quantum Chem. **15**, 251 (1981).

[35] M. H. Beck, A. Jäckle, G. A. Worth, and H. D. Meyer. Physics Reports **324**, 1 (2000).

[36] G. A. Worth, H.-D. Meyer, H. Köppel, L. S. Cederbaum, and I. Burghardt. Int. Rev. Phys. Chem. **27**, 569 (2008).

[37] G. A. Worth, M. H. Beck, A. Jäckle, and H.-D. Meyer, The MCTDH Package, Version 8.4 (2007). See http://mctdh.uni-hd.de.

[38] J. Y. Fang and H. Guo. J. Chem. Phys. **101**, 5813 (1994).

[39] G. A. Worth, H. D. Meyer, and L. S. Cederbaum. J. Chem. Phys. **105**, 4412 (1996).

[40] J. C. Light, I. P. Hamilton, and J. V. Lill. J. Chem. Phys. **82**, 1400 (1985).

[41] R. Kosloff and D. Kosloff. J. Comput. Phys. **63**, 363 (1986).

[42] R. Kosloff and H. Tal-Ezer. Chem. Phys. Lett **127**, 223 (1986).

[43] C. M. Oana and A. I. Krylov. J. Chem. Phys. **127**, 234106 (2007).

[44] Y. Shao, L. Fusti-Molnar, Y. Jung, J. Kussmann, C. Ochsenfeld, S. T. Brown, A. T. Gilbert, L. V. Slipchenko, S. V. Levchenko, D. P. ONeill, R. A. D. tasio Jr., R. C. Lochan, T. Wang, G. J. Beran, N. A. Besley, J. M. Herbert, C. Y. Lin, T. V. Voorhis, S. H. Chien, A. Sodt, R. P. Steele, V. A. Rassolov, P. E. Maslen, P. P. Korambath, R. D. Adamson, B. Austin, J. Baker, E. F. C. Byrd, H. Daschel, R. J. Doerksen, A. Dreuw, B. D. Dunietz, A. D. Dutoi, T. R. Furlani, S. R. Gwaltney, A. Heyden, S. Hirata, C.-P. Hsu, G. Kedziora, R. Z. Khaliullin, P. Klunzinger, A. M. Lee, M. S. Lee, W. Liang, I. Lotan, N. Nair, B. Peters, E. I. Proynov, P. A. Pieniazek, Y. M. Rhee, J. Ritchie, E. Rosta, C. D. Sherrill, A. drew C. Simmonett, J. E. Subotnik, H. L. W. III, W. Zhang, A. T. Bell, A. K. Chakraborty, D. M. Chipman, F. J. Keil, A. Warshel, W. J. Hehre, H. F. S. III, J. Kong, A. I. Krylov, P. M. Gill, and M. Head-Gordon. Phys. Chem. Chem. Phys. (2006).

[45] M. J. Frisch, G. W. Trucks, H. B. Schlegel, G. E. Scuseria, M. A. Robb, J. R. Cheeseman, J. A. Montgomery, Jr., T. Vreven, K. N. Kudin, J. C. Burant, J. M. Millam, S. S. Iyengar, J. Tomasi, V. Barone, B. Mennucci, M. Cossi,

G. Scalmani, N. Rega, G. A. Petersson, H. Nakatsuji, M. Hada, M. Ehara, K. Toyota, R. Fukuda, J. Hasegawa, M. Ishida, T. Nakajima, Y. Honda, O. Kitao, H. Nakai, M. Klene, X. Li, J. E. Knox, H. P. Hratchian, J. B. Cross, V. Bakken, C. Adamo, J. Jaramillo, R. Gomperts, R. E. Stratmann, O. Yazyev, A. J. Austin, R. Cammi, C. Pomelli, J. W. Ochterski, P. Y. Ayala, K. Morokuma, G. A. Voth, P. Salvador, J. J. Dannenberg, V. G. Zakrzewski, S. Dapprich, A. D. Daniels, M. C. Strain, O. Farkas, D. K. Malick, A. D. Rabuck, K. Raghavachari, J. B. Foresman, J. V. Ortiz, Q. Cui, A. G. Baboul, S. Clifford, J. Cioslowski, B. B. Stefanov, G. Liu, A. Liashenko, P. Piskorz, I. Komaromi, R. L. Martin, D. J. Fox, T. Keith, M. A. Al-Laham, C. Y. Peng, A. Nanayakkara, M. Challacombe, P. M. W. Gill, B. Johnson, W. Chen, M. W. Wong, C. Gonzalez, and J. A. Pople, *Gaussian 03, Revision B.05*.

[46] P. J. Derrick, L. Asbrink, O. Edqvist, and E. Lindholm. Spectrochim. Acta **27**, 2525 (1971).

[47] G. R. Wu, A. E. Boguslavskiy, O. Schalk, M. S. Schuurman, and A. Stolow. J. Chem. Phys. **135**, 164309 (2011).

[48] H. Köppel, E. V. Gromov, and A. B. Trofimov. Chem. Phys. **304**, 35 (2004).

[49] D. T. Colbert and W. H. Miller. J. Chem. Phys. (1992).